A New Polarimetric Change Detector in Radar Imagery

Armando Marino, *Member, IEEE*, Shane R. Cloude, *Fellow, IEEE*, and
Juan M. Lopez-Sanchez, *Senior Member, IEEE*

Abstract—In modern society, the anthropogenic influences on ecosystems are central points to understand the evolution of our planet. A polarimetric synthetic aperture radar may have a significant contribution in tackling problems concerning land use change, since such data are available with any-weather conditions. Additionally, the discrimination capability can be enhanced by the polarimetric analysis. Recently, an algorithm able to identify targets scattering an electromagnetic wave with any degree of polarization has been developed, which makes use of a vector rearrangement of the elements of the coherency matrix. In the present work, this target detector is modified to perform change detection between two polarimetric acquisitions, for land use monitoring purposes. Regarding the selection of the detector parameters, a physical rationale is followed, developing a new parameterization of the algebraic space where the detector is defined. As it will be illustrated in the following, this space is 6-D complex with restrictions due to the physical feasibility of the vectors. Specifically, a link between the detector parameters and the angle differences of the eigenvector model is obtained. Moreover, a dual polarimetric version of the change detector is developed, in case quad-polarimetric data are not available. With the purpose of testing the methodology, a variety of data sets were exploited: quad-polarimetric airborne data at L-band (E-SAR), quad-polarimetric satellite data at C-band (Radarsat-2), and dual-polarimetric satellite data at X-band (TerraSAR-X). The algorithm results show agreement with the available information about land changes. Moreover, a comparison with a known change detector based on the maximum likelihood ratio is presented, providing improvements in some conditions. The two methodologies differ in the analysis of the total amplitude of the backscattering, where the proposed algorithm does not take this into consideration.

Index Terms—Change detection, polarimetry, synthetic aperture radar (SAR).

I. INTRODUCTION

IN ORDER to understand comprehensively the evolution of our planet, accurate land monitoring is indispensable. Satellite systems seem to suit better these requirements due to their extensive and constant coverage. Additionally, radar images can be acquired with reasonable independence on the

weather conditions. The latter property is revealed as a winning advantage to achieve time series of data. Moreover, the analysis of the polarization of the electromagnetic waves scattered by targets in the scene [1]–[3] enhances significantly the discrimination capabilities with respect to single polarization acquisitions. The work presented in this paper is aimed at developing a polarimetric change detector (PCD). The PCD would be able to detect areas (or generally targets) in the scene for which the observed polarimetric characteristics suffered a change between the two acquisitions. The more direct application of a PCD is the identification of areas that suffered changes due to human or natural interventions. Classical examples could be forest logging, woodland fires, or flooding. Operatively, a PCD may be exploited in conjunction with a geographical information system (GIS) database to perform disaster or illegal activities monitoring. On the other hand, a different application of a PCD (as it will be better explained in the following) is as a preprocessing step for methodologies exploiting time series of polarimetric SAR acquisitions that require a stability of the target characteristics in the scene. In the case of polarimetric and interferometric synthetic aperture radar (POLInSAR), this requirement is often referred as equi-scattering mechanism.

In the following, a very brief introduction to target polarimetry is presented, focusing mainly on the mathematical tools exploited in the development of the proposed change detector.

A single target is any target scattering an electromagnetic wave having a fixed polarization in time/space. It can be characterized using the scattering (Sinclair) matrix [1], [2]

$$[S] = \begin{bmatrix} HH & HV \\ VH & VV \end{bmatrix} \qquad (1)$$

where H stands for linear horizontal and V for linear vertical (therefore the HV image is obtained transmitting a linear vertical polarization and receiving the linear horizontal one). Equivalently, a formalism based on the scattering vector can be exploited

$$\underline{k} = \frac{1}{2} Trace\left([S]\Psi_2\right) = [k_1, k_2, k_3, k_4]^T \qquad (2)$$

where $Trace(.)$ is the sum of the diagonal elements of the matrix inside, and Ψ_2 is a complete set of 2×2 basis matrices under a Hermitian inner product [1], [2]. In the case that the transmitter and receiver antennas are the same (i.e., monostatic) and the observed target is reciprocal the scattering matrix is symmetric (i.e., $HV = VH$) and only 3 complex numbers are needed to characterize a single target. Therefore, the

four-dimensional scattering vector can be substituted with a 3-D one. For the sake of brevity, in this paper, the hypothesis of a symmetric scattering matrix will be assumed. However, the latter hypothesis is not necessary for the derivation of the detector and an extended version, covering the nonreciprocal and bistatic case, can be easily obtained. Finally, it is possible to define a scattering mechanism as a normalized vector $\underline{\omega} = \underline{k}/\|\underline{k}\|$. The latter unitary vector is defined in a special unitary 3-D complex space (SU(3)) and represents an ideal polarimetric target where the total amplitude backscattered (the span of the scattering matrix) is unitary.

Generally, the targets observed by a SAR system are not ideal scattering mechanisms, but a combination of different objects which we refer to as *partial* targets [4]. To characterize a partial target, a single scattering matrix $[S]$ is not sufficient, since this is a stochastic process and second-order statistics are required [1]–[3]. In this context the target covariance matrix can be estimated

$$[C] = \langle \underline{k}\underline{k}^{*T} \rangle \tag{3}$$

where $\langle \rangle$ is the finite averaging operator. In general, if the scattering vector in a generic basis is $\underline{k} = [k_1, k_2, k_3]^T$, where $k_1, k_2, k_3 \in \mathbb{C}$, the covariance matrix is

$$[C_3] = \begin{bmatrix} \langle |k_1|^2 \rangle & \langle k_1 k_2^{*T} \rangle & \langle k_1 k_3^{*T} \rangle \\ \langle k_1^{*T} k_2 \rangle & \langle |k_2|^2 \rangle & \langle k_2 k_3^{*T} \rangle \\ \langle k_1^{*T} k_3 \rangle & \langle k_2^{*T} k_3 \rangle & \langle |k_3|^2 \rangle \end{bmatrix}. \tag{4}$$

In the literature, when $\underline{k}$ is expressed in the Pauli basis (i.e., $\underline{k} = (1/\sqrt{2})[HH + VV, HH - VV, 2^*HV]^T$), the covariance matrix takes the name of coherency matrix $[T]$ [1]–[3]. However, the matrix $[T]$ and $[C]$ are unitarily similar, therefore they contain the same information and they can be both exploited in the following formulation.

The methodology proposed in this paper takes advantage of the polarimetric coherence. If two different scattering mechanisms, $\underline{\omega}_1$ and $\underline{\omega}_2$, are considered, the polarimetric coherence is

$$\gamma_p = \frac{\underline{\omega}_1^{*T}[C]\underline{\omega}_2}{\sqrt{\left(\underline{\omega}_1^{*T}[C]\underline{\omega}_1\right)\left(\underline{\omega}_2^{*T}[C]\underline{\omega}_2\right)}}. \tag{5}$$

In the case of two polarimetric acquisitions (i.e., two polarimetric images acquired from different positions and/or different times), two scattering vectors can be retrieved: $\underline{k}_1$ and $\underline{k}_2$. The polarimetric coherence in (5) can then be substituted by a mixed polarimetric and interferometric coherence as shown in [5], [6]

$$\gamma_{12} = \frac{\underline{\omega}_1^{*T}[\Omega_{12}]\underline{\omega}_2}{\sqrt{\left(\underline{\omega}_1^{*T}[T_{11}]\underline{\omega}_1\right)\left(\underline{\omega}_2^{*T}[T_{22}]\underline{\omega}_2\right)}} \tag{6}$$

where $[T_{11}] = \langle \underline{k}_1 \underline{k}_1^{*T} \rangle$, $[T_{22}] = \langle \underline{k}_2 \underline{k}_2^{*T} \rangle$ and $[\Omega_{12}] = \langle \underline{k}_1 \underline{k}_2^{*T} \rangle$.

In the following, the symbol $[T]$ will be used exclusively for the coherency matrix (i.e., Pauli basis), while $[C]$ denotes a generic covariance matrix in any basis. In this paper, the coherence in (6) will be estimated exploiting coherency matrices due to their wide utilization in the literature (but again other bases could be exploited).

Many algorithms have been developed to tackle the problem of change detection [7], [8]. Among the procedures exploiting radar polarimetry, one of the most utilized is the Maximum Likelihood ratio (LR) of the two acquisitions [9]. If $[T_{11}]$ and $[T_{22}]$ are the two coherency matrices, the test can be easily built defining $[T] = ([T_{11}] + [T_{22}])/2$ and calculating the ratio

$$R_\Delta = \frac{\sqrt{Det\left([T_{11}]\right)Det\left([T_{22}]\right)}}{Det\left([T]\right)} \tag{7}$$

where $Det([T])$ is the matrix determinant, and R_Δ is defined between 0 and 1. If the ratio is close to unity then no change has occurred.

The latter methodology was selected since it is fast and beneficial and therefore, provides a simple way to compare the results of the proposed approach with detection masks obtained with a methodology fundamentally different from the one exploited in this paper. The differences between the LR methodology and the proposed change detector are mainly two. First of all, the LR approach is based on the statistical distribution of the polarimetric data and is focused on differences on the distributions, whereas the proposed one exploits the polarimetric information of the data. As a consequence, differences are expected between the two detections results. Secondly, in the calculation of the matrix determinants the overall amplitude of the backscattering (i.e., $Trace([T])$) has a significant contribution. This last aspect is helpful when differences in amplitude correspond to target changes. In such a case, the proposed detector will not be able to pick the amplitude differences and can be complemented with the LR methodology (or a threshold on the Span of the scattering matrix). However, in general the amplitude is very sensitive to other factors as changes in the dielectric constant (e.g., in vegetation due to wetness of the weather conditions) and inaccurate radiometric calibration. Therefore, a change detector relying excessively on amplitude may present some undesired false alarms. In conclusion, with the proposed detector there is an opportunity to exclude these changes and benefit from a separated treatment between polarimetry and amplitude. The change detector proposed in this paper is based on a partial target detector, previously developed by the authors [10]–[12], and depends exclusively on the polarimetric information, excluding the overall amplitude. For this reason, the proposed algorithm is independent of the overall amplitude as well. In this sense, it is complementary to the LR ratio mentioned above. As a final remark, it has to be said that the LR methodology exploited here is originally derived from early works in [13] (which takes also into account the issue related with the number of looks employed). Clearly, the full maximum likelihood approach as presented in [13] can be used for quantitative decision boundaries, however it will not change the main ideas and conclusions derived from the comparison.

The organization of the text is as follows. First, the partial target detector based on a perturbation analysis will be presented. Having obtained a general formulation of the detector, the algorithm is modified to accomplish change detection. Specifically, two versions are proposed to take into account quad and dual polarization polarimetry. Subsequently, the issue of setting the selectivity of the detector is tackled to detect changes of

different magnitude. A mathematical formulation is pursued that is able to link the differences of the scattering mechanism with the detector parameters. In this paper, a physical rationale was followed and a parameterization of the change detector is devised. Specifically, the test is set on the base of changes on the parameters of the eigenvector model [14]. Once the parameters can be set, the algorithm is applied to real data to test its performance. In particular, a relatively large variety of data, ranging from airborne to satellite, and with different frequencies, is employed for this purpose. A comparison with the LR ratio is also discussed.

II. PARTIAL TARGET DETECTOR

The aim of this section is to outline the development of a general detector for partial targets, exploiting the same methodology (i.e., perturbation analysis) of the single target detector presented in [15]. More details on the partial target detector can be found in [10], [11]. The first step to obtain an extension of the single target detector is to introduce a vector formalism where each partial target can be uniquely defined with one vector. Starting from (4), a feature partial scattering vector is introduced [10], [11]

$$\underline{t} = Trace\left([C]\Psi_3\right) = [t_1, t_2, t_3, t_4, t_5, t_6]^T =$$
$$= \left[\langle|k_1|^2\rangle, \langle|k_2|^2\rangle, \langle|k_3|^2\rangle, \langle k_1^{*T}k_2\rangle, \langle k_1^{*T}k_3\rangle, \langle k_2^{*T}k_3\rangle\right]^T \quad (8)$$

where Ψ_3 is a complete set of 3×3 basis matrices under a Hermitian inner product and $\underline{t}$ represents all the information of a coherence matrix $[C]$ (6 independent complex numbers) in a vector formalism. Therefore, $\underline{t}$ is defined in a subspace of $\mathbb{C}^6$ and has the first three elements real positive and the second three complex, since the $[C]$ matrix is Hermitian semi positive definite. In the following, the norm of the vector $\underline{t}(\sigma = |\underline{t}|)$ will be referred to as the *overall amplitude*. Any partial target can be characterized by a unique partial vector $\underline{t}$, therefore the partial target that we are interested in the detection can be characterized with this formalism with the symbol $\underline{t}_T$. The latter can be any vector of $\mathbb{C}^6$ in the subspace of the physically feasible ones (again its first three elements real positive and the second three complex). More formally, $\underline{t}_T$ could be expressed as

$$\underline{t}_T = Trace\left([C_T]\Psi_3\right) = [t_{T1}, t_{T2}, t_{T3}, t_{T4}, t_{T5}, t_{T6}]^T \quad (9)$$

where $[C_T]$ represents the covariance matrix of the target of interest. To apply the same processing introduced in [15] for single targets, a perturbed version of $\underline{t}_T$ can be obtained $\underline{t}_P$. This operation can be accomplished by slightly rotating the $\underline{t}_T$ in the space of physically feasible targets. The subsequent step is to perform a change of basis which makes the target of interest to lie only on one component: $\underline{t}_T = \sigma_T[1, 0, 0, 0, 0, 0]^T$, where σ_T represents the norm of $\underline{t}_T(\sigma_T = \|\underline{t}_T\|)$. The latter operation can again be accomplished by multiplications with rotation matrices in the 6-D space. Please note, care must be taken selecting the rotation matrix, since there are rotation matrices that can transform the vector outside the space of physical feasibility. However, it can be demonstrated that any vector in the subspace of physical feasibility can be transformed by a rotation into the first axis of the basis. In the following, we will make use of a normalized version of the vector $\underline{t}_T$, defined

as $\hat{\underline{t}}_T = (\underline{t}_T/\sigma_T)$. In such basis the unitary perturbed target is expressed as $\hat{\underline{t}}_P = [a, b, c, d, e, f]^T$, where $a, b, c \in \mathbb{R}^+$, $|d| \leq \sqrt{ab}$, $|e| \leq \sqrt{ac}$, $|f| \leq \sqrt{bc}$ and $a \gg b, c, |d|, |e|, |f|$. In [15] the detector is built as a weighted inner product between $\underline{\omega}_T$ and $\underline{\omega}_P$ (the two scattering mechanisms). To obtain this in the 6-D space of the partial targets, we can build a matrix $[A]$ exploiting a basis of $\mathbb{C}^6$ built employing a Gram-Schmidt ortho-normalization where the first axis is represented by the vector $\hat{\underline{t}}_T$[16]. If $\underline{u}_1 = \hat{\underline{t}}_T$, $\underline{u}_2$, $\underline{u}_3$, $\underline{u}_4$, $\underline{u}_5$ and $\underline{u}_6$ represent the ortho-normal basis, we can build a diagonal matrix $[A]$ with the observed partial target $\underline{t}$ expressed in the new Gram-Schmidt basis: $[A] = diag(\hat{\underline{t}}_T^{*T}\underline{t}, \underline{u}_2^{*T}\underline{t}, \underline{u}_3^{*T}\underline{t}, \underline{u}_4^{*T}\underline{t}, \underline{u}_5^{*T}\underline{t}, \underline{u}_6^{*T}\underline{t},)$. The linear product between the target and its perturbed version can be simply defined as $\hat{\underline{t}}_T\hat{\underline{t}}_P^{*T}$. To weight the inner product for the target observed in the data, we can multiply each vector for the matrix $[A]$. To conclude, the weighted inner product can be defined as $\langle[A]\hat{\underline{t}}_T\rangle^{*T}\langle[A]\hat{\underline{t}}_P\rangle$:

$$\gamma_q = \frac{\hat{\underline{t}}_T^{*T}[P]\hat{\underline{t}}_P}{\sqrt{\left(\hat{\underline{t}}_T^{*T}[P]\hat{\underline{t}}_T\right)\left(\hat{\underline{t}}_P^{*T}[P]\hat{\underline{t}}_P\right)}} =$$
$$= \frac{1}{\sqrt{1 + \frac{b^2}{a^2}\frac{P_2}{P_1} + \frac{c^2}{a^2}\frac{P_3}{P_1} + \frac{|d|^2}{a^2}\frac{P_4}{P_1} + \frac{|e|^2}{a^2}\frac{P_5}{P_1} + \frac{|f|^2}{a^2}\frac{P_6}{P_1}}} \quad (10)$$

where $[P] = \langle[A]\rangle^{*T}\langle[A]\rangle = diag(|\hat{\underline{t}}_T^{*T}\underline{t}|^2, |\underline{u}_2^{*T}\underline{t}|^2, |\underline{u}_3^{*T}\underline{t}|^2, |\underline{u}_4^{*T}\underline{t}|^2, |\underline{u}_5^{*T}\underline{t}|^2, |\underline{u}_6^{*T}\underline{t}|^2,)$. To make this more readable the following formal substitution is performed: $[P] = diag(P_1, P_2, P_3, P_4, P_5, P_6)$. γ_q is a real number defined between 0 and 1. To have unbiased results the elements of $\hat{\underline{t}}_P$ have to be chosen as $b = c = |d| = |e| = |f|$ [10].

With bias it is meant an imbalance in the weight assigned to each of the covariance matrix elements. In such case, some elements of $[C]$ will have more importance in the evaluation of changing than others. This is clear from (10), where $b = c = |d| = |e| = |f|$ appear in the detector as factors multiplied to the elements of the covariance matrix. We leave as a future work an analysis of whether different weighting of the elements may improve the detection capabilities.

If the clutter components are renamed as $P_c = P_2 + P_3 + P_4 + P_5 + P_6$, the target as $P_T = P_1$, and the ratio $b^2/a^2 = RedR$, the detector can be simplified

$$\gamma_q = \frac{1}{\sqrt{1 + RedR\frac{P_c}{P_T}}} = \frac{1}{\sqrt{1 + RedR\left(\frac{\underline{t}^{*T}\underline{t}}{|\underline{t}^{*T}\hat{\underline{t}}_T|^2} - 1\right)}}. \quad (11)$$

The signal-to-clutter ratio (SCR) can be defined as

$$SCR = \frac{P_T}{P_c} = \left(\frac{\underline{t}^{*T}\underline{t}}{|\underline{t}^{*T}\hat{\underline{t}}_T|^2} - 1\right)^{-1}. \quad (12)$$

The detector is finalized by setting a threshold on γ_q as

$$H_0 : |\gamma_q(P_T, P_c)| \geq T \quad H_1 : |\gamma_q(P_T, P_c)| < T. \quad (13)$$

Details regarding the selection of the parameters $RedR$ and T for a single-acquisition partial target detector can be found in [10].

III. CHANGE DETECTOR

The aim of this section is to modify the previous algorithm to perform change detection between two different acquisitions. The algorithm presented in the previous section can detect a specific polarimetric target (i.e., a reference target), selected on the base of a theoretical model or trained on real data. The main idea of the change detector is to employ the partial vector of the first acquisition as a reference target for a detection executed on the second acquisition. Therefore, if $[T_{11}]$ and $[T_{22}]$ correspond to the coherency matrices of first and second acquisitions, the target to detect is $\underline{t}_1 = Trace([T_{11}]\Psi_3)$ (with $\hat{\underline{t}}_1$ its normalized version), and the target under test is $\underline{t}_2 = Trace([T_{22}]\Psi_3)$.

The polarimetric change detector (PCD) expression can be easily obtained starting from (11) and formally submitting $\hat{\underline{t}}_T = \hat{\underline{t}}_1$ and $\underline{t} = \underline{t}_2$

$$\Gamma_q = \frac{1}{\sqrt{1 + RedR\left(\frac{\underline{t}_2^{*T}\underline{t}_2}{|\underline{t}_2^{*T}\hat{\underline{t}}_1|^2} - 1\right)}} \geq T. \qquad (14)$$

The detector parameters $RedR$ and T still have to be set on the base of some rationale. The subsequent sections deal with this issue.

A. Dual Polarimetric Change Detector

Before proceeding with the setting of the detector parameters, in this subsection a particularization of the test is introduced. The algorithm proposed in the previous section exploits quad polarimetric SAR data. In actual fact, quad polarimetric data are needed to characterize uniquely a partial target. However, in some practical instances, the acquisition of quad polarimetric data can be excessively expensive or impracticable. Often in such cases a single transmit polarization is used with dual coherent receivers measuring orthogonal components of the scattered wave. Such cases we will refer to as dual polarimetric [1], [2].

The methodology exploited to derive the proposed change detector is based on a generic algebraic manipulation (a weighted and normalized inner product), therefore, it can be easily adapted to different typologies of data, as long as the observables can be represented with vectors in an Euclidean space [16]. Moreover, the following mathematical development is presented as an example of the general methodology exploited to derive a detector working on a different algebraic linear space. For instance, a different formalism for the quad polarimetric detector could obtained by rearranging the elements of the Muller matrix in a 9-D real vector (in case of symmetric scattering matrix).

When only two polarimetric channels are available, a 2-D scattering vector can be observed: $\underline{k}_d = [k_1, k_2]^T$, with $k_1, k_2 \in \mathbb{C}$[1], [2]. Subsequently, $\underline{k}_d$ can be exploited to build a 2×2 covariance matrix

$$[C_d] = \begin{bmatrix} \langle|k_1|^2\rangle & \langle k_1^{*T}k_2\rangle \\ \langle k_2^{*T}k_1\rangle & \langle|k_2|^2\rangle \end{bmatrix}. \qquad (15)$$

A 3-D partial feature vector can then be built

$$\underline{t}_d = Trace([C_d]\Psi_2) = \left[\langle|k_1|^2\rangle, \langle|k_2|^2\rangle, \langle k_1^{*T}k_2\rangle\right]^T. \qquad (16)$$

Again, the partial vectors must be measured in the two acquisitions: $\underline{t}_{d1}$ and $\underline{t}_{d2}$, and the first partial vector must be normalized as $\hat{\underline{t}}_{d1} = \frac{\underline{t}_{d1}}{\|\underline{t}_{d1}\|}$.

The dual polarimetric change detector is then expressed as

$$\Gamma_d = \frac{1}{\sqrt{1 + RedR_d\left(\frac{\underline{t}_{d2}^{*T}\underline{t}_{d2}}{|\underline{t}_{d2}^{*T}\hat{\underline{t}}_{d1}|^2} - 1\right)}} \geq T_d. \qquad (17)$$

The problem of setting the parameters $RedR_d$ and T_d is treated in the following sections.

IV. PARAMETERIZATION AND PARAMETERS SETTING

A. Parameterization

The change detector developed in the previous sections has two free parameters, $RedR$ and T, which allow the tuning of the detector selectivity. The aim of this section is to find a criterion able to set them starting from some requirement on the minimum change to detect.

One of the advantages of utilizing partial vectors in $\mathbb{C}^6$ is that *any* partial target can be uniquely identified with a vector rather than a 3×3 matrix. However, due to the novelty of the detector, a parameterization of such space has not been devised yet, and we cannot link vectors in $\mathbb{C}^6$ with scattering mechanisms in SU(3). With such a link, a change in SU(3) would be easily linked with a change of the partial vector, allowing the derivation of a rationale for setting the detector parameters.

Considering that there are two free detector parameters (i.e., $RedR$ and T), one of them, the threshold T, can be theoretically set arbitrarily in the interval $]0, 1[$ (and without any particular rationale). The value chosen in this paper is $T = T_d = 0.9$. Therefore, the following part of the section will be focused on the setting of $RedR$ (after the value $T = T_d = 0.9$ is selected).

First, a parameterization for quad polarimetric data is devised, leaving the treatment of dual polarimetric data for a later section. The modification of the scattering mechanism can be represented with a rotation of the single target in SU(3) (since the scattering mechanism are unitary) [17]. Given $\underline{\omega}_1$, a generic single target in the first acquisition, the basis of the space can be chosen to express $\underline{\omega}_1 = [1, 0, 0]^T$. The scattering mechanism observed in the second acquisition is defined as $\underline{\omega}_2$. Considering $\underline{\omega}_2$ is unitary, an easy way to represent it in the new basis is by polar coordinates

$$\underline{\omega}_2 = [\cos\theta, \sin\theta\cos\varphi e^{j\nu}, \sin\theta\sin\varphi e^{j\tau}]^T. \qquad (18)$$

It is important to note that this formalism matches with the Cloude–Pottier eigenvector model in case that $\underline{\omega}_1$ is a surface or odd bounce scattering mechanism [1]. The first step in developing an algorithm able to detect changes of scattering mechanism in two acquisitions is to select an algebraic operator able to evaluate differences between two scattering mechanisms, $\underline{\omega}_1$

and $\underline{\omega}_2$, in SU(3). The normalized inner product is selected for its generality [16]. Additionally, it is invariant with respect to the vector norm, keeping the advantages of a treatment based exclusively on polarimetry

$$\Delta = \left| \underline{\omega}_1^{*T} \underline{\omega}_2 \right| = \cos \theta \in \mathbb{R}. \tag{19}$$

A parameterization able to express Δ in the $\mathbb{C}^6$ partial target space (where the detector works) is required. The expressions of $\hat{\underline{t}}_1$ and $\underline{t}_2$ can be derived from the coherency matrices of the two scattering mechanisms. These are calculated exploiting the outer product of $\underline{\omega}_1$ and $\underline{\omega}_2$

$$\underline{\omega}_1 \to \underline{\omega}_1 \underline{\omega}_1^{*T} = \begin{bmatrix} 1 & 0 & 0 \\ 0 & 0 & 0 \\ 0 & 0 & 0 \end{bmatrix} \to \underline{t}_1 = \hat{\underline{t}}_1$$
$$= [1, 0, 0, 0, 0, 0]^T, \tag{20}$$

$$\underline{\omega}_2 \to \underline{\omega}_2 \underline{\omega}_2^{*T} \to \underline{t}_2 = \begin{bmatrix} \cos^2 \theta \\ \sin^2 \theta \cos^2 \varphi \\ \sin^2 \theta \sin^2 \varphi \\ \cos \theta \sin \theta \cos \varphi e^{-j\nu} \\ \cos \theta \sin \theta \sin \varphi e^{-j\tau} \\ \sin^2 \theta \cos \varphi \sin \varphi e^{j(\nu-\tau)} \end{bmatrix}. \tag{21}$$

Clearly, the coherency matrices derived from $\underline{\omega}_1$ and $\underline{\omega}_2$ have unitary rank, since they represent coherent (or deterministic) targets, therefore they do not need averaging.

Substituting $\hat{\underline{t}}_1$ and $\underline{t}_2$ in the expression of the SCR we obtain

$$SCR = \frac{\cos^4 \theta}{det} \tag{22}$$
$$det = \sin^4 \theta \cos^4 \varphi + \sin^4 \theta \sin^4 \varphi + \cos^2 \theta \sin^2 \theta \cos^2 \varphi$$
$$+ \cos^2 \theta \sin^2 \theta \sin^2 \varphi + \cos^4 \theta \cos^2 \varphi \sin^2 \varphi. \tag{23}$$

After some algebraic manipulations, the SCR can be simplified to

$$SCR =$$
$$\frac{\cos^4 \theta}{\sin^4 \theta \left(\cos^4 \varphi + \sin^4 \varphi\right) + \cos^2 \theta \sin^2 \theta + \cos^4 \theta \cos^2 \varphi \sin^2 \varphi}. \tag{24}$$

The SCR depends on θ and φ (two rotation angles in polarization space). θ is selected by the requirements on $\left| \underline{\omega}_1^{*T} \underline{\omega}_2 \right|$, whereas there are no requirements concerning φ (rotation around $\underline{\omega}_1$ that does not change the distance of the two scattering mechanisms). Our approach consists in adopting the worst scenario, in this way any random choice of φ will return an equal or smaller detector Γ_q (therefore these points will be automatically discarded). The maximization of Γ_q can be accomplished maximizing the SCR over φ [18]

$$\varphi_M = \max_{\varphi \in [0, 2\pi]} \Gamma_d = \max_{\varphi \in [0, 2\pi]} SCR, \tag{25}$$
$$\forall \varphi \neq \varphi_M : SCR(\varphi) < SCR(\varphi_M). \tag{26}$$

The minimization of the reciprocal of SCR, defined as CSR, can be preferred since it is more straightforward

$$\varphi_M = \max_{\varphi \in [0, 2\pi]} SCR = \min_{\varphi \in [0, 2\pi]} \frac{1}{SCR} = \min_{\varphi \in [0, 2\pi]} CSR. \tag{27}$$
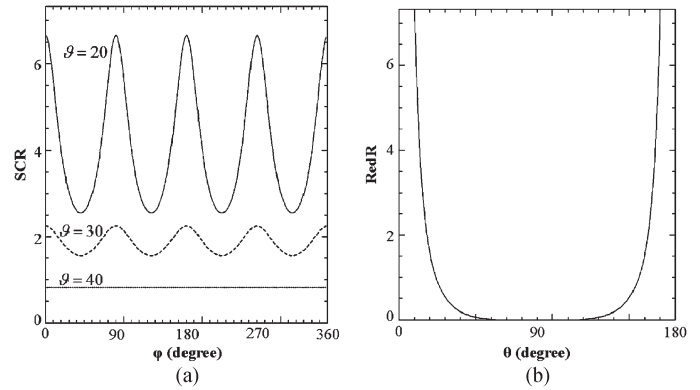

Fig. 1. (a) SCR varying $\varphi \in [0, 360]$. Solid line: $\theta = 20°$; Dashed line: $\theta = 30°$; Dotted line: $\theta = 40°$; (b) $RedR$ varying θ for $\varphi = \varphi_M$.

The search for the minimum is accomplished with the rule of the derivatives

$$\frac{\partial CSR}{\partial \varphi} = 0 \Rightarrow \sin(4\varphi_M) = 0 \Rightarrow \varphi_M = n \frac{\pi}{2}. \tag{28}$$

The second derivative is used to assess when a critical point is a maximum or a minimum. In particular, for $\tan^4 \theta < 0.5$ (i.e., θ smaller than about 40°) the maxima of SCR are $\varphi_M = 0$, $\varphi_M = (1/2)\pi$, $\varphi_M = \pi$ and $\varphi_M = (3/2)\pi$. On the other hand, for $\tan^4 \theta > 0.5$ the maxima of SCR are $\varphi_M = (1/4)\pi$, $(3/4)\pi$, $(5/4)\pi$ and $(7/4)\pi$. For $\theta \sim 40$ degree the SCR is constant with respect to φ.

Fig. 1(a) shows the plot of the SCR, where φ is varied for a fixed θ. The plots confirm that the maxima are located in φ_M and the values of SCR is constant for $\theta \sim 40$ degree.

Once fixed $\varphi_M = 0$, the expression of the SCR can be simplified to

$$SCR = \frac{\cos^4 \theta}{\sin^4 \theta + \cos^2 \theta \sin^2 \theta} = \frac{\cos^4 \theta}{\sin^2 \theta} \tag{29}$$

which is an expression depending only on θ. Subsequently, starting from (14) the expression of the $RedR$ can be set utilizing the values of SCR and T

$$RedR = SCR \left(\frac{1}{T^2} - 1 \right). \tag{30}$$

To illustrate common parameter values, Table I shows the $RedR$ and SCR for four choices of angle θ (degrees). Again the threshold is set as $T = 0.9$.

Finally, Fig. 1(b) depicts the trend of $RedR$ varying angle θ. Therefore, if particularly small changes are of interest (small θ angle), the value of RedR to be chosen becomes very high. In the detector, this will increase the components perpendicular to $\hat{\underline{t}}_1$, therefore a detection will be accomplished only if these components are very small (i.e., $\underline{t}_2$ and $\hat{\underline{t}}_1$ very similar, for exception of the overall amplitude). The plot also shows a symmetric behavior with a reflection around angle $\pi/2$. This is expected, since the direction of the scattering mechanism can be included in its absolute phase and hence neglected in the characterization of the target. For instance, two vectors with an angle difference of π (i.e., a minus sign) represent the same scattering mechanism.

TABLE I
PARAMETERS FOR COHERENT CHANGE OF SCATTERING MECHANISM

θ (degree)	RedR	SCR
0	∞	∞
10	7.32	31.19
20	1.56	6.67
30	0.53	2.25

B. Interpretation of the Distance Between Two $\underline{\omega}$

In the previous section, the detector parameters were linked to the scattering mechanisms differences through a parameterization. However, the angular distance between two scattering mechanisms does not yet have a straightforward physical interpretation. The aim of this section is to provide a physical/algebraic interpretation of the θ angle. The model selected to represent the scattering mechanism is the Cloude–Pottier eigenvector model, due to its straightforward geometrical significance [1], [2], [19]. However, other parameterizations could be exploited [19].

The two scattering mechanisms are

$$\underline{\omega}_1 = [\cos\alpha_1, \sin\alpha_1 \cos\beta_1 e^{j\mu_1}, \sin\alpha_1 \sin\beta_1 e^{j\epsilon_1}]^T$$
$$\underline{\omega}_2 = [\cos\alpha_2, \sin\alpha_2 \cos\beta_2 e^{j\mu_2}, \sin\alpha_2 \sin\beta_2 e^{j\epsilon_2}]^T. \quad (31)$$

θ corresponds to the modulus of the inner product $|\underline{\omega}_1^{*T}\underline{\omega}_2|$. After the scalar product is performed, the trigonometric product-to-sum formulas can be exploited to find the expression

$$\underline{\omega}_1^T\underline{\omega}_2^* = \frac{1}{2}\left[\cos\Delta\alpha + \cos\Sigma\alpha + \frac{1}{2}(\cos\Delta\alpha - \cos\Sigma\alpha)\right.$$
$$\times (\cos\Delta\beta + \cos\Sigma\beta)e^{j\Delta\mu} + \frac{1}{2}$$
$$\left.\times (\cos\Delta\alpha - \cos\Sigma\alpha)(\cos\Delta\beta - \cos\Sigma\beta)e^{j\Delta\epsilon}\right]$$
$$= \cos\theta e^{j\zeta} \quad (32)$$

where $\Delta\alpha = \alpha_2 - \alpha_1$, $\Delta\beta = \beta_2 - \beta_1$, $\Sigma\alpha = \alpha_2 + \alpha_1$ and $\Sigma\beta = \beta_2 + \beta_1$. After a few manipulations, we can obtain the expression

$$\cos\theta e^{j\zeta} = \frac{1}{2}\left[\cos\Delta\alpha + \cos\Sigma\alpha + \frac{1}{2}(\cos\Delta\alpha - \cos\Sigma\alpha)\right.$$
$$\left.\times \left[\cos\Delta\beta(e^{j\Delta\mu} + e^{j\Delta\epsilon}) + \cos\Sigma\beta(e^{j\Delta\mu} - e^{j\Delta\epsilon})\right]\right]. \quad (33)$$

To simplify the calculations, the hypothesis $\Delta\mu = \Delta\epsilon = \Delta\phi$ is assumed. In fact, μ and ϵ do not have a straightforward physical interpretation, and it is reasonable to consider a change which does not prefer one phase difference with respect to the other. Please note, this position does not state that μ and ϵ have

the same value, but merely that their variations must be in both cases higher than $\Delta\phi$ to set a detection

$$\cos\theta e^{j\zeta} = \frac{1}{2}\left(\cos\Delta\alpha + \cos\Sigma\alpha + \cos\Delta\alpha\cos\Delta\beta e^{j\Delta\phi}\right.$$
$$\left. - \cos\Sigma\alpha\cos\Delta\beta e^{j\Delta\phi}\right) = A. \quad (34)$$

The final purpose of these calculations is to find an expression of θ depending exclusively on the angle differences of the eigenvector model and not on their actual value. In this way, the test would be general and applicable to any $\underline{\omega}$. The expression in (34) depends on α_1, since $\Sigma\alpha$ is a function of α_1, even when the difference $\Delta\alpha$ is kept constant (i.e., $\Sigma\alpha = 2\alpha_1 + \Delta\alpha$). To remove this dependence, an averaged expression over all the possible α_1 angles can be considered [18]. This is performed analytically exploiting the normalized integral varying the angles but keeping their difference constant (i.e., $\Delta\alpha = const$)

$$\cos\tilde{\theta}e^{j\tilde{\zeta}} = \frac{2}{\pi}\int_0^{\frac{\pi}{2}} A\,d\alpha_1 \quad (35)$$

since $\alpha_1 \in [0, \pi/2]$. To simplify the formalism, in the following the symbol θ will be employed to refer to $\tilde{\theta}$. Considering that

$$\frac{2}{\pi}\int_0^{\frac{\pi}{2}} \cos(2\alpha_1 - \Delta\alpha)d\alpha_1 = \frac{2}{\pi}\sin\Delta\alpha \quad (36)$$

the result of the integral is

$$\cos\theta e^{j\zeta} = \frac{1}{2}\left(\cos\Delta\alpha + \frac{2}{\pi}\sin\Delta\alpha + \cos\Delta\alpha\cos\Delta\beta e^{j\Delta\phi}\right.$$
$$\left. - \frac{2}{\pi}\sin\Delta\alpha\cos\Delta\beta e^{j\Delta\phi}\right). \quad (37)$$

We are interested in the modulus of the inner product. To derive this expression the following equalities can be considered:

$$|\cos\theta e^{j\zeta}| = \cos\theta = \sqrt{(\Re(\cos\theta e^{j\zeta}))^2 + (\Im(\cos\theta e^{j\zeta}))^2}$$
$$e^{j\Delta\phi} = \cos\Delta\phi + j\sin\Delta\phi. \quad (38)$$

Therefore

$$\cos\theta = \frac{1}{2}\left[\left(\cos\Delta\alpha + \frac{2}{\pi}\sin\Delta\alpha\right)^2\right.$$
$$+ \cos^2\Delta\phi\cos^2\Delta\beta\left(\cos\Delta\alpha - \frac{2}{\pi}\sin\Delta\alpha\right)^2$$
$$+ 2\cos\Delta\beta\cos\Delta\phi\left(\cos\Delta\alpha - \frac{2}{\pi}\sin\Delta\alpha\right)$$
$$\times \left(\cos\Delta\alpha + \frac{2}{\pi}\sin\Delta\alpha\right) + \cos^2\Delta\beta\sin^2\Delta\phi$$
$$\left.\times \left(\cos\Delta\alpha - \frac{2}{\pi}\sin\Delta\alpha\right)^2\right]^{\frac{1}{2}}. \quad (39)$$

TABLE II
VALUES OF θ VARYING THE ANGLES (DEGREE),
FOR QUAD POLARIMETRIC DATA

$\Delta\alpha$	$\Delta\beta$	$\Delta\phi$	θ	$RedR$
0	0	0	0	∞
4	4	4	5.25	27.50
9	9	9	11.70	5.25
16	16	16	20.41	1.49
25	25	25	30.89	0.48
27	27	27	34.16	0.35
30	30	30	36.26	0.28

Collecting terms and exploiting the relationship $(a - b)(a + b) = a^2 - b^2$, a final expression can be derived

$$
\cos\theta = \frac{1}{2}\left[\left(\cos\Delta\alpha + \frac{2}{\pi}\sin\Delta\alpha\right)^2 + \cos^2\Delta\beta\right.
$$

$$
\times \left(\cos\Delta\alpha - \frac{2}{\pi}\sin\Delta\alpha\right)^2 + 2\cos\Delta\beta\cos\Delta\phi
$$

$$
\left. \times \left(\cos^2\Delta\alpha - \frac{4}{\pi^2}\sin^2\Delta\alpha\right)\right]^{\frac{1}{2}}. \tag{40}
$$

With this final expression we have obtained a link between the model angle differences and the θ angle, which enables a physical rationale for setting θ. The latter is strictly related with the detector through the SCR (as shown in the previous section). Table II represents some values of θ obtained with the model angle differences.

C. Dual-Pol Parameterization

This section is concerned with the setting of the parameter $RedR_d$ for the dual polarimetric change detector. Again the threshold is arbitrarily set as $T_d = 0.9$.

To relate the values of Γ_d to physical changes, a parameterization of the $\mathbb{C}^3$ space of the partial targets $\underline{t}_d$ is needed. A change of the dual polarimetric scattering mechanism $\underline{\omega}_d$ can still be represented with a rotation. Given $\underline{\omega}_{d1}$, a generic single target in the first acquisition, the basis can be chosen to express $\underline{\omega}_{d1} = [1, 0]^T$. A generic scattering mechanism in the second acquisition is defined as $\underline{\omega}_{d2}$. Again $\underline{\omega}_{d2}$ is represented in the new basis by polar coordinates: $\underline{\omega}_{d2} = [\cos\theta, \sin\theta e^{j\zeta}]^T$. The normalized inner product is chosen to evaluate the differences between $\underline{\omega}_{d1}$ and $\underline{\omega}_{d2}$

$$
\Delta = \left|\underline{\omega}_{d1}^{*T}\underline{\omega}_{d2}\right| = \cos\theta \in \mathbb{R}. \tag{41}
$$

A parameterization able to link Δ to the change detector is required. The dual polarimetric coherency matrices can be defined with the outer product of $\underline{\omega}_d$ as $[C_d] = \langle\underline{\omega}_d\underline{\omega}_d^{*T}\rangle$. The expressions of $\underline{\hat{t}}_{d1}$ and $\underline{t}_{d2}$ is derived as $\underline{\hat{t}}_{d1} = [1, 0, 0]^T$ and $\underline{t}_{d2} = [\cos^2\theta, \sin^2\theta, \cos\theta\sin\theta e^{j\zeta}]^T$. Substituting $\underline{\hat{t}}_{d1}$ and $\underline{t}_{d2}$ in the expression of SCR we obtain

$$
SCR = \frac{\cos^4\theta}{\sin^4\theta + \cos^2\theta\sin^2\theta} = \frac{\cos^4\theta}{\sin^2\theta} \tag{42}
$$

which is interestingly the same expression found in (29). The expression in (42) provides a link between SCR and the angle differences between two generic dual polarimetric scattering mechanism. Subsequently, $RedR_d$ can be set utilizing (30).

D. Interpretation of the Dual Polarimetric Distance for HH/VV

In this section, a physical interpretation of θ in the case of dual polarimetric HH/VV data is provided. The model selected to represent the scattering mechanism is again the eigenvector model [1]. Please note, the model can only be applied if the two co-polarizations are acquired. In dual polarimetric data only a subspace of the entire SU(3) can be observed and part of the parameters of the quad polarimetric eigenvector model cannot be inverted unambiguously. The solution exploited in this paper is to neglect these parameters. Specifically, neglecting β a reflection symmetric space is assumed. This hypothesis does not constitute a loss of generality of the proposed algorithm, since it is intrinsic of dual polarimetric acquisitions (in our case HH/VV). If physical changes take place in the complex line orthogonal to the complex plane spanned by the two vectors (e.g., HH and VV), they cannot be observed anyway (i.e., quad polarimetry is required to observe these changes). The two scattering mechanisms are

$$
\underline{\omega}_{d1} = [\cos\alpha_1, \sin\alpha_1 e^{j\zeta_1}]^T
$$

$$
\underline{\omega}_{d2} = [\cos\alpha_2, \sin\alpha_2 e^{j\zeta_2}]^T. \tag{43}
$$

The derivation proceed as for the quad polarimetric case. After the scalar product, the trigonometric product-to-sum formulas and the integration can be utilized to find the expression

$$
\left|\omega_{d1}^T\omega_{d2}^*\right| = \frac{1}{2}\left[\left(\cos\Delta\alpha + \frac{2}{\pi}\sin\Delta\alpha\right.\right.
$$

$$
\left. + \left(\cos\Delta\alpha - \frac{2}{\pi}\sin\Delta\alpha\right)\cos\Delta\zeta\right)^2
$$

$$
\left. + \left(\cos\Delta\alpha - \frac{2}{\pi}\sin\Delta\alpha\right)^2\sin^2\Delta\zeta\right]^{\frac{1}{2}} \tag{44}
$$

where $\Delta\alpha = \alpha_2 - \alpha_1$ and $\Delta\zeta = \zeta_2 - \zeta_1$. After some more manipulations a simpler expression can be found

$$
\left|\omega_{d1}^T\omega_{d2}^*\right| = \frac{1}{2}\left[4\cos^2\Delta\alpha + 2\right.
$$

$$
\left. \left(\cos^2\Delta\alpha - \frac{4}{\pi^2}\sin^2\Delta\alpha\right)(\cos\Delta\zeta - 1)\right]^{\frac{1}{2}}. \tag{45}
$$

TABLE III
DETECTOR PARAMETERS VARYING THE ANGLES (DEGREE)
FOR DUAL POLARIMETRIC HH/VV DATA

$\Delta\alpha$	$\Delta\zeta$	θ	$RedR_d$
0	0	0	∞
5	5	5.59	24.28
10	10	11.16	5.81
15	15	16.68	2.39
20	20	22.18	1.21
25	25	27.53	0.68

Finally, considering that $|\omega_{d1}^T \omega_{d2}^*| = \cos\theta$ a link between $RedR$ and the angle differences $\Delta\alpha$, $\Delta\zeta$ is found. Table III presents $RedR$ for different values of $\Delta\alpha$ and $\Delta\zeta$.

V. REAL DATA VALIDATION

In this section, the proposed algorithms are tested over real data. To provide a relatively large validation, different typologies of data were considered, including airborne and satellite systems, with different resolutions, frequencies, and polarimetric modes.

A. Polarimetric Data Description

First, airborne data are exploited, since they provide higher resolution and signal-to-noise ratio compared to the other data sets. The data were acquired in 2006 by the German Aerospace Center (DLR) with the E-SAR airborne system, during the SARTOM campaign [20]. The acquisitions employed in this validation are in L-band with a resolution of 1.5 m in slant range and 0.9 m in azimuth (the pixel sampling is 1.5 m and 0.44 m). The L-band data set was chosen since it is quad polarimetric and presents a low-frequency foliage penetration capability when compared to other sensors exploited in the following sections. One of the aims of the SARTOM project was target detection under forest cover. For this reason, several targets were deployed inside and outside the forest. Additionally, some of the targets were removed in later acquisitions. Therefore, the data set represents an ideal scenario for testing the proposed algorithm.

The second data set considered was acquired by RADARSAT-2 (MDA) in 2009. This is in C-band with resolution of 5.4 m in slant range and 8.0 m in azimuth (the sampling is 4.7 m in range and 5.1 m in azimuth). The exploitation of Radarsat-2 data allows to test a different frequency with coarser resolution. The data were acquired in Canada (Indian Head, Saskatchewan) in the framework of the AgriSAR2009 campaign [21]. This was a ESA campaign to study polarimetric time-series on agricultural fields. Accurate ground measurements of the fields were carried out during the acquisitions. The images employed in this particular test were acquired on 11th of August and 04th of September 2009 (24 days of temporal baseline) with an incidence angle of 34°.

Finally, TerraSAR-X (DLR) dual-pol HH/VV X-band data are employed. The resolution here is 1.18 m in slant range and 6.6 m in azimuth, while the sampling is 0.91 m in range and 2.39 m in azimuth. As pointed out previously, the use of quad polarimetric data is generally preferred due to the higher discrimination capability. However, in some instances only dual polarimetric data are available. In particular, the combination of the co-polar channels HH and VV seems to be more advantageous than the use of the cross-polarized channel HV, at least with this sensor. The scene consists of a rural area (mainly rice fields) close to Seville (Spain). Two acquisitions are used here, gathered on the 17th and 28th of May 2009, hence at the beginning of the rice cultivation season. The incidence angle is 30°.

B. E-SAR L-Band Quad Polarimetric Data

The first experiment considers two acquisitions where the slave was acquired 4 days after with a zero spatial baseline. This is an ideal test for the proposed PCD, since only temporal effects are visible. Fig. 2(a) and (b) present the corresponding Pauli RGB color composite image (Red: $|HH - VV|$; Green: $2|HV|$; Blue: $|HH + VV|$). A ground truth campaign was carried out during the acquisitions. The scene is a mix of forest stands and open field areas. Specifically, the bright points (and geometrical shapes) in open field areas are man-made targets (e.g., vehicles and metallic nets). The open field area was mainly covered by grass with sparse bushes. Moreover, weather conditions were slightly different at these two dates: a rainy day in the master acquisition, and just a wet day (without rain) for the slave. The targets that were not present in the second acquisition are indicated with circles on the RGB images.

The coherency matrices for the two acquisitions T_{11} and T_{22} were estimated via spatial averaging. In this example, 121 samples were averaged, which corresponds to an Equivalent Number of Looks (ENL) of 59. The result of the algorithm is a coherence mask (Γ_q), where the values are linearly scaled between the threshold $(T = 0.9)$ and 1. The detection mask is presented in Fig. 3(a), where the angle differences is $\Delta\alpha = \Delta\beta = \Delta\mu = \Delta\epsilon = 27°$. Consequently, all the black areas experienced changes that modified the model angles more than $27°$. All the removed targets appear as dark spots in the mask. Clearly, several other points are below the threshold. This is because the purpose of the algorithm is to detect all the areas that suffered changes in the scattering mechanisms between the two acquisitions and not just man-made targets.

To have an idea about the performances of the proposed PCD, another widely utilized test, the LR ratio of coherency matrices determinants is illustrated in Fig. 3(b). The threshold employed here is 0.8, which is a lower value compared to the commonly exploited in the literature (which is 0.9) [9]. This is because here the algorithm is focused exclusively on changes due to the removal of point targets, which are supposed to be relatively significant. Therefore, the use of a lower threshold would reduce the number of false alarms. However, in the following experiments the more common value of 0.9 will be exploited. Again, it is important to keep in mind that the two detectors are focused on different aspects of the data, therefore
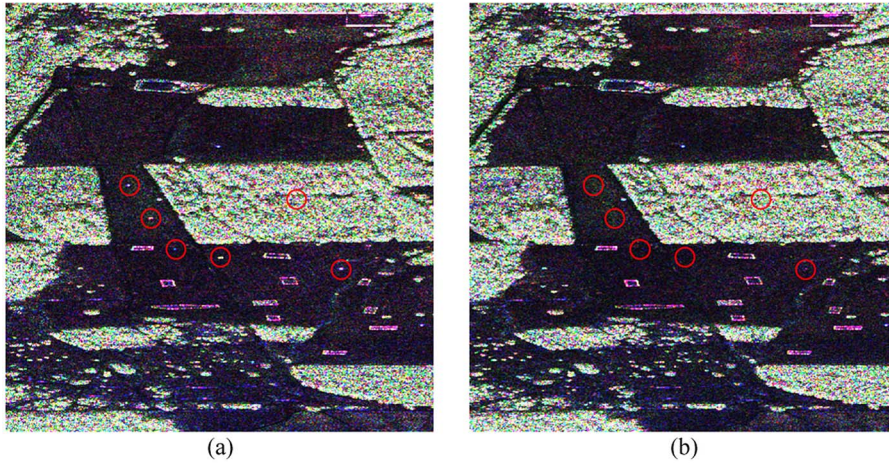
Fig. 2.   RGB Pauli composite images with E-SAR L-band data. (a) first acquisition: Master; (b) second acquisition after 4 days (zero baseline): Slave 1.
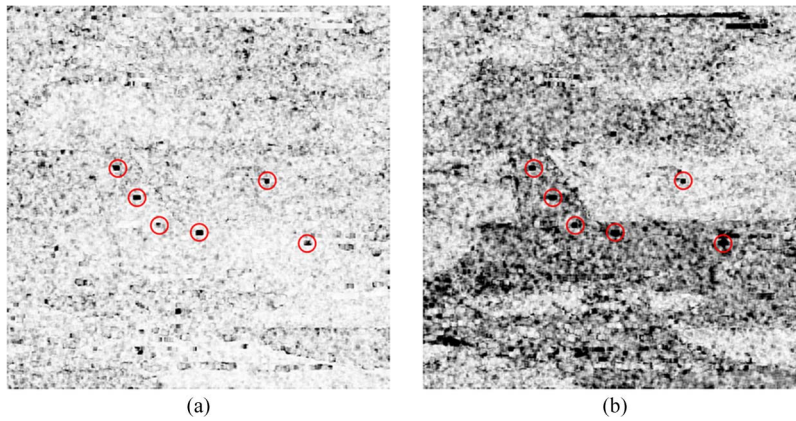

Fig. 3.   Polarimetric change detection on E-SAR L-band data. ENL: 59. (a) Proposed PCD with $\Delta\alpha = \Delta\beta = \Delta\mu = \Delta\epsilon = 16°$. (b) LR ratio test with threshold 0.8.
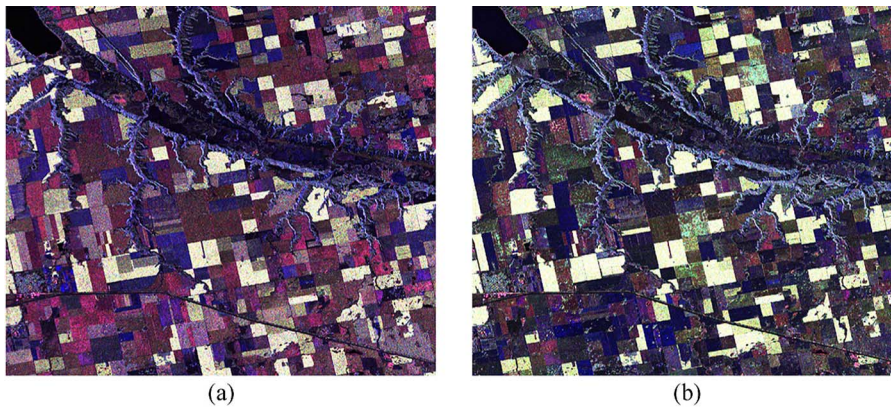

Fig. 4.   RGB Pauli image of the Radarsat-2 scene in Indian Head: (a) first acquisition; (b) second acquisition.

we expect some differences. Now, the open field presents the largest changes, and most areas are below the threshold. In this area there were not changes in the scattering mechanisms during the 4 days, however the overall backscattered amplitude is different due to changes in wetness conditions of the ground (i.e., dielectric constant). As expected, the change in amplitude is detected by the LR algorithm. Instead, this effect is not present in the proposed PCD [recall Fig. 2(a) and (b)]. Regarding the detection of changes to point targets, the LR test does

not seem to be suited as well, due to its sensitivity to the overall intensity.

C. Radarsat-2 Fine Quad Polarimetric Data

Fig. 4 presents the RGB Pauli composite images of the two acquisitions. To make the pixel of the RGB image almost square on the ground, a preliminary polarimetric multilook of 4×2 (azimuth $\times$ range) is performed. Before to run the algorithm
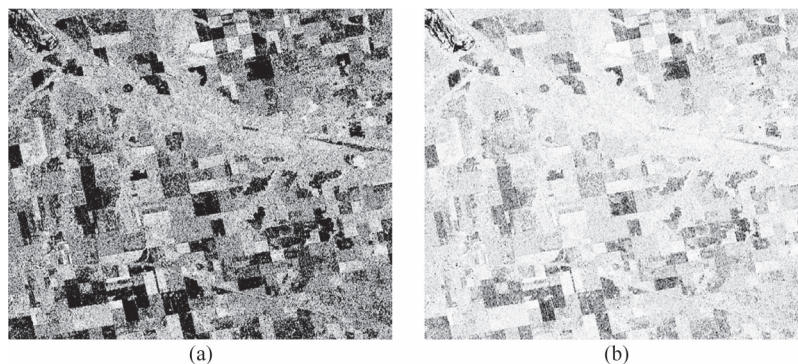
Fig. 5. Change detection with Radarsat-2 data in Indian Head. $ENL = 110$ (a) $\Delta\alpha = \Delta\beta = \Delta\mu = \Delta\epsilon = 16°$; (b) $\Delta\alpha = \Delta\beta = \Delta\mu = \Delta\epsilon = 27°$.
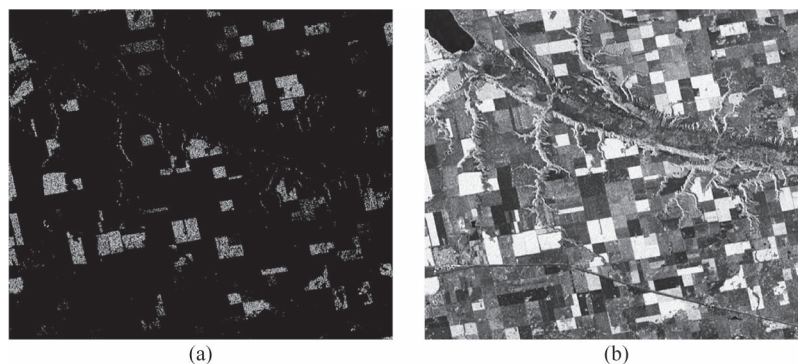

Fig. 6. LR test for Radarsat-2 data in Indian Head. $ENL = 110$. (a) Threshold 0.9; (b) no threshold.

a coregistration procedure for the images was performed. The scene is composed of agricultural parcels of different sizes where different crop types are cultivated, with a lake in the upper left corner. The small dark spots in the right hand side are small ponds.

Fig. 5(a) and (b) show the detection masks for angle differences of $\Delta\alpha = \Delta\beta = \Delta\mu = \Delta\epsilon = 16°$ and $\Delta\alpha = \Delta\beta = \Delta\mu = \Delta\epsilon = 27°$, respectively. Coherency matrices were estimated by averaging 200 samples, resulting in an ENL of 110. Most of the crop fields are above the threshold, but there is also a significant number with a dark or black mask. This is in line with the preliminary results of the campaign discussed in [21], since at the date of these acquisitions part of the crops in the area were developing quickly, whereas other maintained similar phenological stages. The fields below the threshold are easily identified on the RGB images, since it is clear how their color (hue) has changed significantly. Please note, on the RGB image only changes in color are related to polarimetric changes (i.e., changes in the scattering mechanisms), whereas changes in brightness are directly related to amplitude (span) variations.

A comparison with the LR ratio of matrix determinants is also provided. The mask in Fig. 6(a) is linearly scaled between 0.9 and 1 (i.e., equivalent to a threshold equal to 0.9). The test shows that almost all the fields are under the 0.9 requirement. To have a better understanding of this result, the LR ratio is also presented without any threshold, simply scaled between 0 and 1, in Fig. 6(b). Most of the scene is relatively dark and only few bright fields are visible.

To have a better look at the changes, a smaller area is analyzed next. The RGB Pauli images of this area are presented in Fig. 7. From the images it is clear that some of the parcels exhibit a visible change whereas others seem to remain stable. To have an additional insight of the polarimetric properties, the entropy (scaled between 0 and 1) and α angle (scaled between 0 and $\pi/2$) are shown in Figs. 8 and 9, respectively. The detection mask for $16°$ angle difference with the PCD and the LR ratio without threshold are also presented in Fig. 10.

For illustration purposes, we focus our analysis in three rectangles with different behavior on this area (see location in Fig. 7).

1) Green rectangle on the upper left part. Here, the PCD does not detect consistent changes whereas it is relatively low for the LR ratio (around 0.4). To check if polarimetric changes took place between the two acquisitions, the entropy and α images are exploited, estimating an average value within the considered parcel. Interestingly, entropy remains stable in both acquisitions, with values of 0.61 and 0.67, respectively, for the lower right corner (bluish parcel, which corresponds to a lentil field), and 0.80 to 0.81 for the rest (which correspond to parcels cultivated with flax and spring wheat). Regarding the α angle, this passes from 25 to $27°$ in the bluish part and stay stable at $38°$ in the rest. These changes are very small and much below the limit of $16°$ that we imposed. To understand the reason of the low LR ratio, a closer look at the RGB images reveals a quite significant change in the overall amplitude. The span (i.e., sum of the diagonal terms of the coherency matrix) varies from about 1 dB to
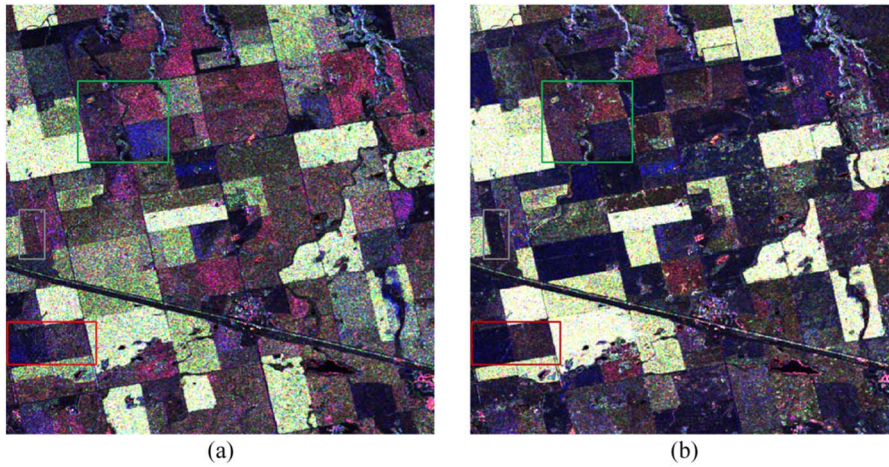
Fig. 7. RGB Pauli image of the Radarsat-2 data in Indian Head (small area). (a) First acquisition; (b) second acquisition.
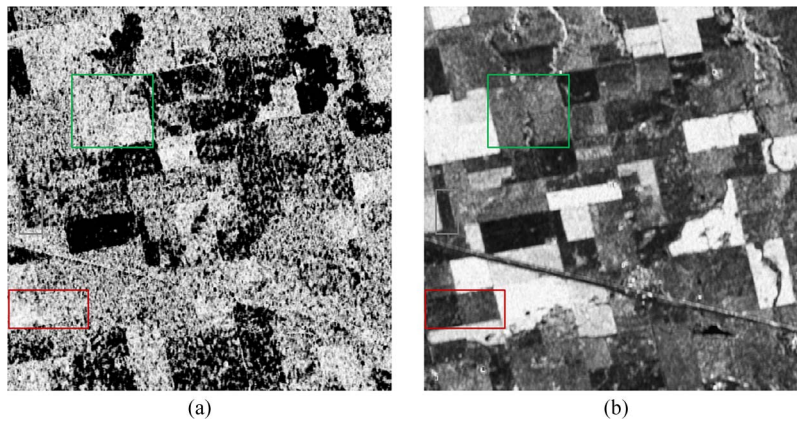

Fig. 8. Change detection with Radarsat-2 data in Indian Head (small area). $ENL = 110$ (a) $\Delta\alpha = \Delta\beta = \Delta\mu = \Delta\epsilon = 16°$; (b) LR without threshold.
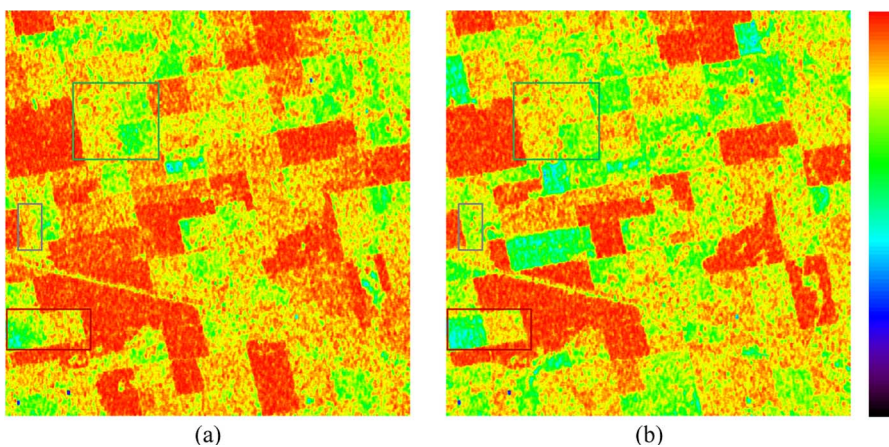

Fig. 9. Entropy images with Radarsat-2 data in Indian Head (small area), scaled between 0 and 1. $ENL = 110$ (a) first acquisition; (b) second acquisition.

−6 dB in the bluish parcel and from 1.6 dB to −5 dB in the rest.

2) Red rectangle in the lower left corner. As for the previous case the LR ratio is particularly low: 0.3 for the right parcel (flax) and 0.21 for left parcel (fallow), while the proposed algorithm does not detect consistent changes. A closer look at the entropy reveals that it stays stable to 0.82 in the right parcel and varies from 0.49 to 0.59 in the left one. Regarding the α parameter, this changes

from 40 to 38° for the right and from 22 to 18° for the left parcel. As a conclusion, the polarimetric characteristic of the two fields are not changing significantly. Regarding the analysis of the span, the second acquisition presents a consistent lower scattering from 1.7 dB to −6 dB for the right and from 0.98 dB to −8 dB for the left parcel.

3) Gray rectangle in the left side (spring wheat). In this situation both the PCD and the LR ratio detect changes (the latter is approximate 0.16). The study of this parcel
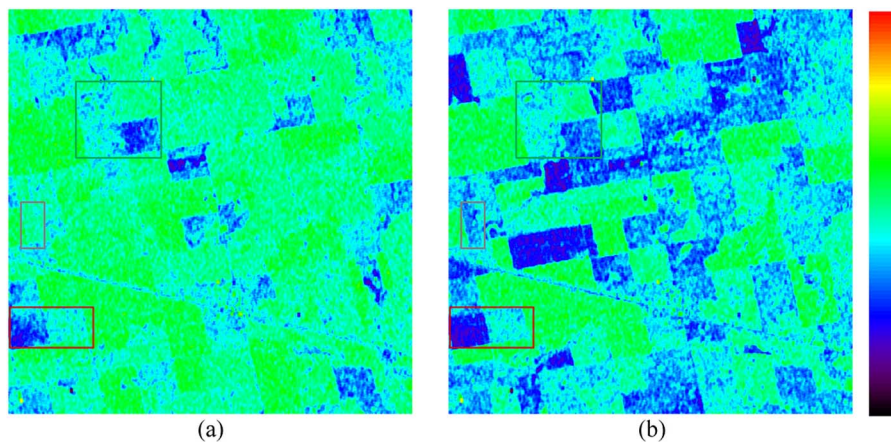
Fig. 10. Alpha angle images with Radarsat-2 data in Indian Head (small area), scaled between 0 and $\pi/2$. $ENL = 110$ (a) first acquisition; (b) second acquisition.
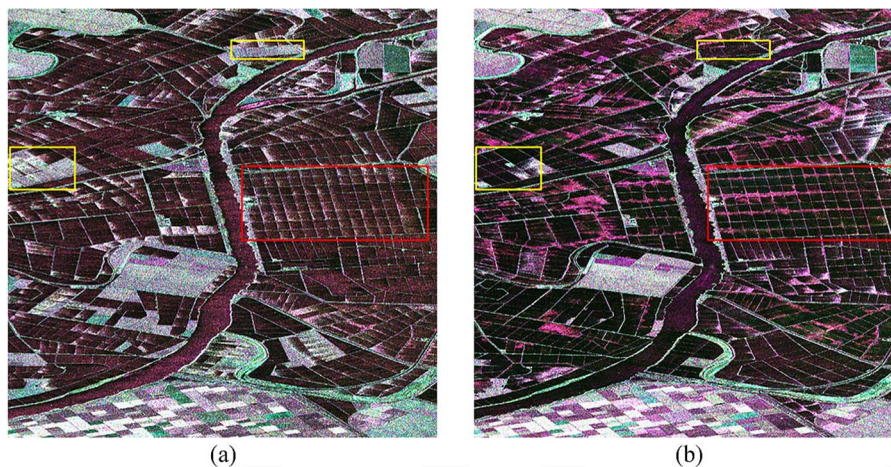

Fig. 11. RGB image of TerraSAR-X of agricultural area (mainly rice). Red: C_{11}, Blue: C_{22}, Green: T_{22}: (a) first acquisition (17th May 2009); (b) second acquisition (28th May 2009).
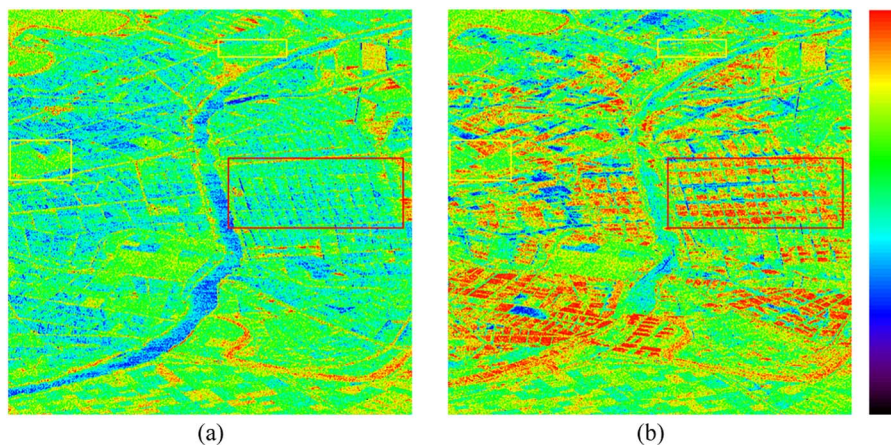

Fig. 12. Entropy images with TerraSAR-X. $ENL = 109$: (a) first acquisition (17th May 2009); (b) second acquisition (28th May 2009).

is interesting since the PCD detector seems to be proximal to the threshold, with several parcel areas above and other below. To understand this result, entropy and α angle can be analyzed. Its entropy changes from about 0.85 to 0.73, and the α angle passes from 45 to 31°. These large changes in α (14°) and entropy justify the partial detection of these spots within the parcel. In fact, the α difference is just around the threshold of 16° and the statistical variation along the parcel returns the fluctuating behavior of the detector.
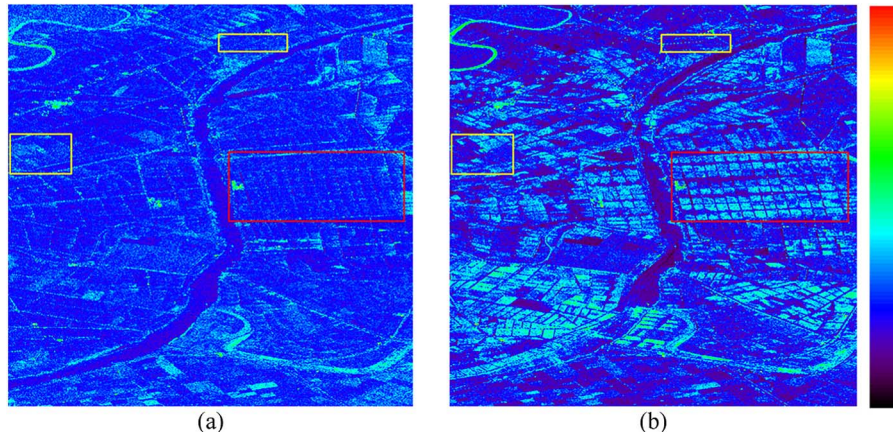
Fig. 13. α angle images with TerraSAR-X. $ENL = 109$: (a) first acquisition (17th May 2009); (b) second acquisition (28th May 2009).
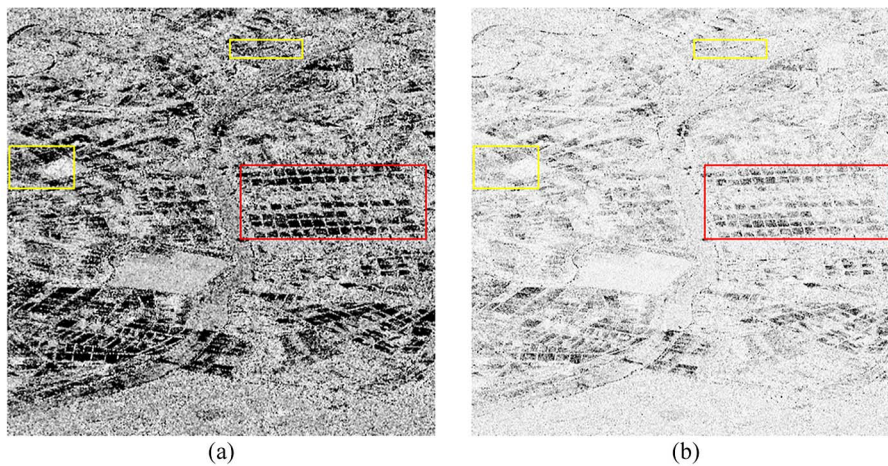

Fig. 14. Change detection masks. Linear scaling from 0.9 to 1. $ENL = 109$: (a) $\Delta\alpha = \Delta\zeta = 18°$. (b) $\Delta\alpha = \Delta\zeta = 28°$.
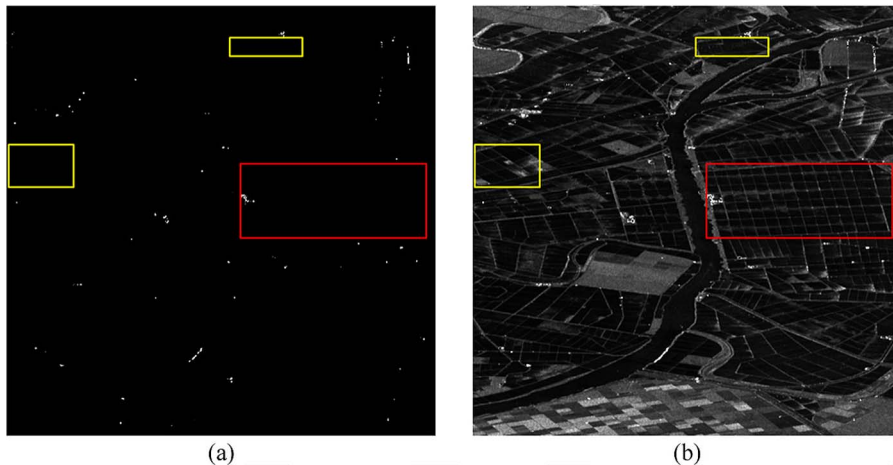

Fig. 15. Change detection with LR ratio. $ENL = 109$: (a) $T = 0.9$; (b) absence of threshold.

D. TerraSAR-X Dual Polarimetric Data HH/VV

In this section, the algorithm is tested with dual polarimetric HH/VV TerraSAR-X data. The RGB images of the two acquisitions are presented in Fig. 11(a) and (b), respectively. The color coding of the images is Red: $C_{11} = \langle |HH|^2 \rangle$, Green: $T_{22} = \langle |HH - VV|^2 \rangle$ and Blue: $C_{22} = \langle |VV|^2 \rangle$. The scene presents mainly flooded rice fields (dark areas), with other crops in the lower part, and the Guadalquivir river crossing diagonally. Ground measurements are available over the rice fields. In both the acquisitions the fields are flooded and without plants emerging. However, in the first acquisition some of the fields are still not flooded (they appear as brighter parcels and are indicated with green rectangles in the second RGB). Interestingly, the wind condition in the first acquisition was much

stronger than in the second one. Due to the larger roughness of the water surface, the flooded fields look much brighter, giving an overall intensity difference of about 10 dB between the two acquisitions. More importantly, the backscatter from large parts of the rice fields in the second image was around or below the noise level of the SAR system (with Noise Equivalent Sigma Zero, $NESZ \approx -19$ dB).

In this case, 28×14 pixels were averaged for a total of 392 samples and $ENL = 109$. Compared to the Radarsat-2 data, the ENL is about the same, but the number of samples is much higher due to the large oversampling of the data. Fortunately, the resolution provided by TerraSAR-X data is higher than Radarsat-2, therefore the final resolution is not excessively influenced by the use of many samples. Clearly, the number of samples necessary is dependent on the application. In our case, we are analyzing agricultural fields where the targets of interest are supposed to be relatively distributed on a large area. On the other hand, in urban areas where the targets are supposed to be more coherent and smaller, less samples can be considered.

As in the previous case, the entropy and α angles images, obtained with the dual-pol version of the eigendecomposition, are presented in Figs. 12 and 13 to provide an insight about the polarimetric information content of both acquisitions. The resulting change detection masks are presented in Fig. 14(a) and (b). The angle differences chosen here are (a) $\Delta\alpha = \Delta\zeta = 18°$ and (b) $\Delta\alpha = \Delta\zeta = 28°$. Although the physical interpretation of α angle is the same, variations of α produce different effects on the angle between two generic scattering mechanisms in the two spaces (i.e., θ). The evaluation of the angular difference between the two scattering mechanisms is the focal point of the detector (especially if this result has to be used as a test and exported to other algorithms). To compare the results obtained with dual and quad polarimetric data the test has to be performed utilizing the same θ and therefore the same SCR [as illustrated in (29) and (42)]. This is the reason why the angle differences were selected as 18 and 28° in this case.

Again, the masks are linearly scaled between the threshold $T = 0.9$ and 1, therefore all the gray points passed the test. Several changes can be detected especially with the more restrictive angle difference of 18°. A comparison with the LR is provided in Fig. 15. The LR test is below the threshold almost everywhere in the scene (except for stable isolated scatterers). As introduced before the first acquisition exhibits on average a backscatter level around 10 dB over the second one on the rice areas, and the LR test is strongly affected by this change.

The fields indicated by the red rectangle on the right side are analyzed first. The algorithm detect these pixels as suffering polarimetric changes. An accurate observation of the area reveals that part of the rice parcels start acquiring a different color. Specifically, entropy increases strongly and average α angle goes from low values to 45°. The same comments hold for other similar fields in the scene (not indicated here to do not overfull the image with markers). This change is most probably due to backscattering coefficients being below the noise floor during the second acquisition. In such noisy conditions entropy approaches 1, and for that entropy the average α angle is constrained to be close to 45° by definition in the dual-pol case.

The yellow rectangles (i.e., right side and upper right corner) exhibit clear changes already in the RGB images. In this case these parcels were not flooded during the first acquisition yet, and they corresponded to bare surfaces (without vegetation). Entropy and α angle can be very beneficial to interpret this effect. Both images present a low entropy (around 0.5) and a similar α angle (although the second is closer to 0). Therefore, the two targets (bare ground and rough water surface) appears quite similar from the polarimetric point of view, and hence the PCD is able to see this similarity (this area is well above the threshold). Clearly, this does not happen for the LR ratio test, since the difference in amplitude makes the ratio very close to 0.

VI. CONCLUSION

In this paper, a new polarimetric change detector (PCD) is proposed. The algorithm is based on a previous partial target detector which exploits perturbation filters. The partial targets observed in the first acquisition are employed as reference targets for the detection performed on the second acquisition. To be able to set the threshold, a parameterization is introduced linking the outputs of the detector with the angle differences from the eigenvector model for the coherency matrix. The proposed change detector was tested with a variety of data sets, including airborne and spaceborne sensors with different resolutions, frequencies and polarimetric modes. This detector has been compared with a widely used polarimetric detector, the Maximum Likelihood (LR) ratio of the two acquisitions.

The main advantage of the proposed algorithm seems to be its capability to neglect the overall amplitude of the backscattering, taking into account exclusively the polarimetric information. Mathematically, changes in the overall amplitude are not related to changes of the polarimetric target and generally they are not related to macroscopic physical changes of the target. However, the question regarding the importance of the overall amplitude is still under analysis. One remarkable advantage of the proposed PCD is the possibility to separate the polarimetric information from the overall amplitude. Clearly, if the amplitude is essential in the characterization of the temporal characteristics of a target, a simple threshold detector on the amplitude can be used jointly with the polarimetric one.

REFERENCES

[1] S. R. Cloude, *Polarisation: Applications in Remote Sensing*. London, U.K.: Oxford Univ. Press, 2009.

[2] J. S. Lee and E. Pottier, *Polarimetric Radar Imaging: From Basics to Applications*. Boca Raton, FL: CRC Press, 2009.

[3] W. M. Boerner, *Basics of Radar Polarimetry*, 2004, RTO SET Lecture Series, [Online]. Available: http://envisat.esa.int/polsarpro/Manuals/LN_Basic_Concepts.pdf

[4] G. A. Deschamps and P. Edward, "Poincare sphere representation of partially polarized fields," *IEEE Trans. Antennas Propag.*, vol. AP-21, no. 4, pp. 474–478, Jul. 1973.

[5] K. P. Papathanassiou and S. R. Cloude, "Single-baseline polarimetric SAR interferometry," *IEEE Trans. Geosci. Remote Sens.*, vol. 39, no. 11, pp. 2352–2363, Nov. 2001.

[6] S. R. Cloude and K. P. Papathanassiou, "Polarimetric SAR interferometry," *IEEE Trans. Geosci. Remote Sens.*, vol. 36, no. 5, pp. 1551–1565, Sep. 1998.

[7] J. F. Mas, "Monitoring land-cover changes: A comparison of change detection techniques," *Int. J. Remote Sens.*, vol. 20, no. 1, pp. 139–152, 1999.

[8] R. J. Radke, S. Andra, O. Al-Kofahi, and B. Roysam, "Image change detection algorithms: A systematic survey," *IEEE Trans. Signal Process.*, vol. 14, no. 3, pp. 294–307, Mar. 2005.

[9] L. Ferro-Famil and M. Neumann, "Recent advances in the derivation of POL-inSAR statistics: Study and applications," in *Proc. EUSAR*, 2008, pp. 1–4.

[10] A. Marino, S. R. Cloude, and I. H. Woodhouse, "Detecting depolarized targets using a new geometrical perturbation filter," *IEEE Trans. Geosci. Remote Sens.*, vol. 50, no. 10, pp. 3787–3799, Oct. 2012.

[11] A. Marino, S. R. Cloude, and I. H. Woodhouse, "Detecting depolarizing targets with satellite data: A new geometrical perturbation filter," in *Proc. IGARSS*, 2010, pp. 1847–1850.

[12] A. Marino and S. R. Cloude, "Detecting depolarizing targets using a new geometrical perturbation filter," in *Proc. EUSAR*, Achen, Germany, Jun. 2010, pp. 1–10.

[13] K. Conradsen, A. A. Nielsen, J. Schou, and H. Skriver, "A test statistic in the complex Wishart distribution and its application to change detection in polarimetric SAR data," *IEEE Trans. Geosci. Remote Sens.*, vol. 41, no. 1, pp. 4–19, Jan. 2003.

[14] S. R. Cloude and E. Pottier, "An entropy based classification scheme for land applications of polarimetric SAR," *IEEE Trans. Geosci. Remote Sens.*, vol. 35, no. 1, pp. 68–78, Jan. 1997.

[15] A. Marino, S. R. Cloude, and I. H. Woodhouse, "A polarimetric target detector using the Huynen fork," *IEEE Trans. Geosci. Remote Sens.*, vol. 48, no. 5, pp. 2357–2366, May 2010.

[16] G. Strang, *Linear Algebra and Its Applications*. Mason, OH: Thomson Learn., 1988.

[17] S. R. Cloude, "Electromagnetic Symmetry," in *Lie Groups in EM Wave Propagation and Scattering*. Washington, DC: Taylor & Francis, 1995, ch. 2, pp. 91–142.

[18] K. F. Riley, M. P. Hobson, and S. J. Bence, *Mathematical Methods for Physics and Engineering*. Cambridge, U.K.: Cambridge Univ. Press, 2006.

[19] S. R. Cloude and E. Pottier, "A review of target decomposition theorems in radar polarimetry," *IEEE Trans. Geosci. Remote Sens.*, vol. 34, no. 2, pp. 498–518, Mar. 1996.

[20] R. Horn, M. Nannini, and M. Keller, "SARTOM airborne campaign 2006: Data acquisition report," Microw. Radar Inst. German Aerosp. Res. Centre (DLR), Hechendorf, Germany, DLR-HRSARTOM-TR-001, 2006.

[21] R. Caves and J. Padda, "AgriSAR 2009, data analysis report: Field level database," MDA Syst., Oxford, U.K., Nov. 2010, Tech. Rep.

Armando Marino (M'11) received the M.Sc. degree in telecommunication engineering from the Università di Napoli "Federico II," Naples, Italy, in 2006 and the Ph.D. degree from the University of Edinburgh, Edinburgh, U.K., in 2011, in the field of polarimetric SAR interferometry.

In 2006, he was with the High Frequency and Radar Systems Department (HR), German Aerospace Centre (DLR), Oberpfaffenhofen, where he developed his M.Sc. thesis, which focused on SAR multipass retrieval of forest parameters. From March 2011 to October 2011, he was with the Institute of Computing Research, University of Alicante, Spain. Since December 2011, he has been a Postdoctorate Researcher with the Institute of Environmental Engineering, ETH Zürich, Zürich, Switzerland.

Dr. Marino was a recipient of the "Best Ph.D. Thesis 2011" award by the Remote Sensing and Photogrammetry Society (RSPSoc) and the "Outstanding Ph.D. Thesis" award by Springer-Verlag, which published the thesis in 2012.

Shane R. Cloude (M'87–SM'96–F'01) received the B.Sc. degree from the University of Dundee, Dundee, U.K., in 1981 and the Ph.D. degree from the University of Birmingham, Birmingham, U.K., in 1987.

He was a Radar Scientist with the Royal Signals and Radar Establishment, Great Malvern, U.K., until 1987. He then held teaching and research posts with the University of Dundee, the University of York, U.K., and the University of Nantes, France. Since 1996, he has been the Director and Senior Scientist with Applied Electromagnetic Consultants (AELc), Edinburgh, U.K., undertaking contract research on a range of problems associated with radar remote sensing.

Dr. Cloude is a Fellow of the Alexander von Humboldt Society in Germany.

Juan M. Lopez-Sanchez (S'94–M'00–SM'05) was born in Alicante, Spain, in 1972. He received the Ingeniero and Dr.Ing. degrees in telecommunication engineering from the Technical University of Valencia (UPV), Valencia, Spain, in 1996 and 2000, respectively.

From 1998 to 1999, he was a Predoctoral Grantholder with the Space Applications Institute, Joint Research Centre of the European Commission, Ispra, Italy. Since 2000, he has been leading the Signals, Systems, and Telecommunication Group, University of Alicante, Spain, where he has been a Full Professor since November 2011. He has coauthored more than 40 papers in refereed journals and more than 70 papers and presentations in international conferences and symposia. His main research interests include microwave remote sensing for inversion of biophysical parameters, polarimetric and interferometric techniques, SAR imaging algorithms, and analytical and numerical models for multiple scattering problems.

In 2001, Dr. Lopez-Sanchez was a recipient of the INDRA award for the best Ph.D. thesis about radar in Spain. Since 2006, he has been the Chair of the Spanish Chapter of the IEEE Geoscience and Remote Sensing Society.